Exp Fluids (2007) 43:959–967
DOI 10.1007/s00348-007-0366-3

RESEARCH ARTICLE

Investigation of internal pressure gradients generated in electrokinetic flows with axial conductivity gradients

Shankar Devasenathipathy · Rajiv Bharadwaj · Juan G. Santiago

Received: 17 September 2006 / Revised: 17 July 2007 / Accepted: 17 July 2007 / Published online: 17 August 2007

Abstract Field amplified sample stacking (FASS) is used to increase sample concentrations in electrokinetic flows. The technique uses conductivity gradients to establish a non-uniform electric field that accumulates ions within a conductivity gradient, and can be readily integrated with capillary electrophoresis. Conductivity gradients also cause gradients in near-wall electroosmotic flow velocities. These velocity gradients generate internal pressure gradients that drive secondary, dispersive flows. This dispersion leads to a significant reduction in the efficiency of sample stacking. This paper presents an experimental investigation of internally generated pressure gradients in FASS using micron-resolution particle image velocimetry (μPIV). We measure velocity fields of particles seeded into an electrokinetic FASS flow field in a glass microchannel with a single buffer–buffer interface. μPIV allows for the direct quantification of local, instantaneous pressure gradients by analyzing the curvature of velocity profiles. Measurements show internally generated pressure-driven velocities on the order of 1mm/s for a typical applied electric field of 100 V/cm and a conductivity ratio of 10. A one-dimensional (1D) analytical model for the temporal development of the internal pressure gradient generation is proposed which is useful in estimating general trends in flow dynamics.

S. Devasenathipathy · R. Bharadwaj · J. G. Santiago (✉)
Mechanical Engineering Department, Stanford University,
440 Escondido Mall, Stanford, CA 94305, USA
e-mail: juan.santiago@stanford.edu

Present Address:
S. Devasenathipathy
Intel Corporation, Assembly & Test Technology Development,
5000 W Chandler Blvd, Chandler, AZ 85226, USA

Present Address:
R. Bharadwaj
Caliper Life Sciences, 605 Fairchild Drive,
Mountain View, CA 94043, USA

List of symbols

E	applied electric field
U	liquid velocity
L	length of the channel
α	length of the high conductivity segment (x_D) non-dimensionalized by L
σ	electrolyte conductivity
ν	electroosmotic wall mobility
γ	ratio of electrolyte conductivities

Subscripts

eof	electroosmotic flow
p	pressure-driven flow
eph	electrophoretic
BGE	back ground electrolyte
s	sample zone

1 Introduction

Sensitivity to low (e.g., <10 nM) sample concentrations is often a challenge in the design of on-chip capillary electrophoresis (CE) assays. Techniques to enhance sample concentration limits include field amplified sample stacking (FASS) (Burgi and Chien 1991), free-standing capillary field-amplified sample injection (FASI) (Chien and Burgi 1991), and large volume sample stacking (LVSS) (Chien and Burgi 1992). All of these processes use non-uniform electrolyte conductivity. FASS is a common method in which conductivity gradients are used to create non-uniform electromigration of sample ions and

thereby stack them at the interface between low and high conductivity regions. FASS as an on-chip concentration technique gains particular significance for its simplicity, generality, and ease of integration with electrophoretic separation techniques (Jacobson et al. 1994; Jacobson and Ramsey 1995; Manz et al. 1992). An important challenge in FASS is that non-uniform axial conductivity profiles lead to axial electric field gradients. Non-uniform conductivities lead to non-uniform electric fields (very important) and non-uniform electroosmotic wall mobilities (less important). Both of these lead to significantly non-uniform near-wall electroosmotic flow (EOF) velocities, and the generation of internal pressure gradients which disperse samples and lower concentration efficiency. Other electrokinetic flow with significant conductivity gradients include current monitoring flows (used to quantify electroosmotic mobility) (Huang et al. 1988), thermal gradient focusing (Ross et al. 2001), and isotachophoresis (Wainright 2002).

Burgi and Chien (1991) developed a simple 1-D model for estimating cross-section-area averaged velocity due to internal pressure gradients. They assumed conductivity gradients are constant in time and discontinuous at the interface. They considered a plug of fixed length migrating along the length of the channel. They discuss the effects of pressure driven flow components, which tend to broaden the otherwise sharp zones generated by the stacking process and reduces resolution. Several methods have been suggested to correct for this dispersion. Reduction of EOF channel mobilities by imposing radial electric fields externally (Kasicka 1997) and lowering pH (Quirino and Terabe 1999) has been reported. Another approach for minimizing dispersion is the treatment of channel walls with water-soluble polymers to suppress EOF. Bharadwaj and Santiago (2005) used polyethylene oxide coating to suppress EOF. Bharadwaj and Santiago (2005) and Ren and Li (2006) both showed numerical model results for internally generated pressure driven velocity profiles. However, to our knowledge, no measurements of velocity profiles (or fields) associated with internally-generated pressure gradients have been reported. Such studies should provide insight into the dynamics of electrokinetic flow fields with conductivity gradients.

The current work extends the experimental study of FASS by introducing seed particles into the flow field and tracking the motion of these particles. Devasenathipathy et al. (2002) and Kim et al. (2002) have earlier applied μPIV to study electroosmotically-driven flow fields in homogeneous electrolyte systems. This work contributes towards the understanding of the dynamics of the generation of internal pressure gradient generation by providing depth resolved quantitative measurements of the spatially and temporally developing fluid flow field with axial conductivity gradients. A greater understanding of these flow dynamics is useful in the optimization of FASS.

2 Theory

In on-chip FASS, sample is dissolved in an electrolyte of lower concentration than the background electrolyte. A sample plug is then injected either electrokinetically or with pressure-driven flow into a separation channel, forming conductivity interfaces immediately upstream and downstream of the sample plug (Yang and Chien 2001). Another, also common realization is a single interface configuration (Bharadwaj and Santiago 2005) where the sample and background electrolyte regions fill two axial segments of the entire channel of interest as shown in Fig. 1. In all cases, the low conductivity sample region is a high electrical resistance in series with the rest of the channel. Large electric fields and large electrophoretic velocities (relative to the background electrolyte) are therefore established in the sample region. As ions cross from high to low electrophoretic velocity regions (respectively regions of low and high conductivity), they stack at the interface region. Figure 1 shows schematically the

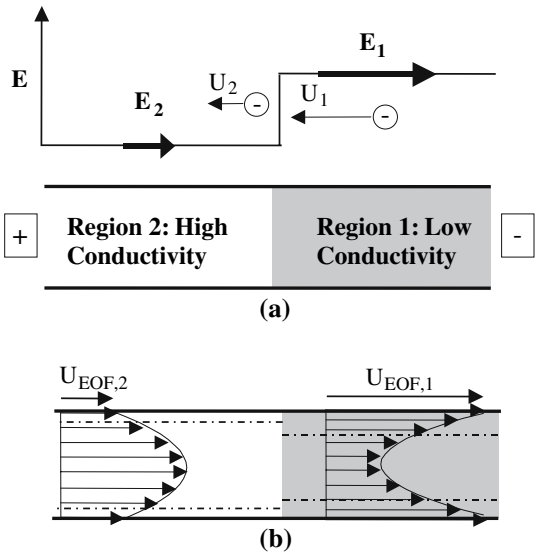

Fig. 1 **a** Schematic of field amplified sample stacking showing the electric field along the channel with superimposed arrows indicating ion motion and (below) shading indicating ion densities and field polarity. In FASS, sample is dissolved in the low conductivity/high electric field segment (Region 1). Anionic species cross the interface of the low-conductivity/high field region (Region 1) and stack in the high conductivity/low electric field segment (Region 2). In this paper, we seed the entire field with fluorescent flow seed particles. **b** Schematic of velocity field showing the internal pressure gradients generated due to a mis-match in electroosmotic velocities in the two segments. In the 1-D model presented here, the interface is treated as a sharp zone of negligible width (compared to channel length) and the flow in each section is treated as one-dimensional

stacking of negative ions at the conductivity interface. The background electrolyte-to-sample zone conductivity ratio, defined as

$$\gamma = \frac{\sigma_{\mathrm{BGE}}}{\sigma_S} \tag{1}$$

typically determines the maximum achievable level of stacking. This term is also referred to as the field enhancement factor in capillary electrophoresis literature. Electroosmotic flow, the motion of the bulk liquid in response to an applied electric field in a liquid channel with electric double layers on its wetted surfaces, is a function of the wall surface chemistry. Under the thin electric double layer approximation, the electroosmotic velocity is related to the electric field through the local value of the electroosmotic (wall) mobility, ν_{eof}

$$U_{\mathrm{EOF}} = \upsilon_{\mathrm{eof}} E. \tag{2}$$

The background-to-sample region electric field ratio is γ^{-1}. The background-to-sample electroosmotic mobility ratio depends on the local field and on the fact that ν_{eof} is a function of local ion concentration and chemistry. For sufficiently high concentrations of the buffers used for the present experiments, we can assume pH is constant so that the main dependence is on ion concentration. We shall model the concentration dependence of electroosmotic mobility as a power law of the form $\nu_{\mathrm{eof}} = \nu_{\mathrm{eof,o}}\, \gamma^{\beta}$ where $\nu_{\mathrm{eof,o}}$ is a reference value and β is an empirically determined parameter dependent on channel surface chemistry and electrolyte solution. β typically ranges between -0.15 and -0.5. Conventional theory (i.e., assuming constant surface charge at the wall), suggests a value of -0.5, but this is well known to over-predict the dependence (e.g., see Hunter 1981). Szymczyk et al. (1999) suggest a value of -0.21 for ceramic porous membrane while Sadr et al. report $\beta = -0.28$ for electroosmotic flow with sodium tetraborate buffer (Sadr 2004). Another correlation for the dependence of electroosmotic mobility on ionic concentration and pH has been proposed by Thormann et al. (1998). In this paper, we assume a value of –0.2 for β, as per Bharadwaj and Santiago (2005).

Incorporating both these effects on electroosmotic flow results in a sample-to-background electrolyte region electroosmotic velocity ratio of the form

$$\frac{U_{\mathrm{eof},S}}{U_{\mathrm{eof,BGE}}} \approx \gamma^{-1.2}. \tag{3}$$

This mismatch in electroosmotic velocity induces internal pressure gradients in the flow field.

In the current experiments, we consider FASS in a rectangular (or square) cross-section microchannel with a single conductivity interface. A schematic of the flow profiles for a single electrolyte–electrolyte interface is shown in Fig. 1. The position x_D is the time-dependent location of the conductivity interface. Far enough from the interface (e.g., five hydraulic diameters or more), fluid velocities can be assumed to be purely axial such that the axial (u) and transverse (v and w) velocity components are respectively $u = u(y,z)$ and $v = w = 0$. This approximation of largely axial velocities is analogous to the lubrication approximation often used in fluid flow analysis (White 1991).

3 1D model for pressure generation

We here present the derivation of a simple one-dimensional (1D) expression for the variation of pressure gradients in a FASS channel in space and time. We assume locally fully-developed flow in a long thin tube of arbitrary cross-section. As described in detail by Chen et al. (2005) and Bharadwaj and Santiago (2005) for similar electrokinetic flows, we assume the net neutrality approximation and that charge accumulation in the channel (outside of the double layers) occurs at time scales much faster than those of the velocity and sample concentration fields. That is, applied electric fields couple with conductivity gradients to generate net charge in the bulk fluid (Lin 2004), but this charge density is negligible compared to total ion concentration. This implies that the main contributions to local ion density are due to Ohmic current and that the conservation of current density can be well approximated as $\nabla \cdot (\sigma \bar{E}) = 0$, where σ is local conductivity and $\bar{E}$ is electric field. For a long-thin channel of uniform cross-section, we can therefore write

$$\sigma_1 E_1 = \sigma_2 E_2 \tag{4}$$

where the subscripts 1 and 2 refer respectively, to the low and high conductivity segments. Equation 4 can be combined with Eq. 1 to yield $E_1 = \gamma\, E_2$.

The sum of the potential drops across the two segments in series is the voltage drop across the length of the channel, $V_0 = V_1 + V_2$, so that

$$E_0 L = E_2 x_D + E_1 (L - x_D). \tag{5}$$

Equation 5 is written in terms of an effective applied electric field, E_0, defined as the voltage drop divided by channel length x_D and $(L-x_D)$ are respectively, the lengths occupied by high and low conductivity segments. The effects of both variable field and buffer concentration results in an electroosmotic velocity which is different in the two buffer segments as specified in Eq. 3. For incompressible liquids, the net fluid flow across each cross-section should be the same, $Q_1 = Q_2$, so the liquid velocity in each segment, $U(y,z)$, is

$$U(y,z) = U_p(y,z) + U_{\text{eof}} \tag{6}$$

where U_{eof} is the local electroosmotic flow and U_p is the (non-uniform) velocity due to pressure driven flow. Here (y,z) are Cartesian coordinates describing axes perpendicular to the flow channel (for some arbitrary long, thin tube). In typical microchannel EOF, the Debye length, λ_d, is much smaller than the characteristic channel dimension; so EOF can be modeled by a slip surface parallel to and within a few Debye lengths of the wall. The details of the double layer need not be treated in detail and the forces within the double layer can be replaced with a slip surface where the slip velocity is everywhere proportional to the local electric field (and local zeta potential). This relation can be thought of as a Helmholtz Smoluchowski equation generalized to the case of non-uniform electric fields and zeta potential (see for example Santiago 2001).

As in the Reynolds equations for lubrication theory, the relevant terms are the near-wall velocities. Here, there is no externally applied pressure differences and the internal pressure gradient supplies a local, non-uniform Poiseuille flow component that maintains a constant flow rate along the channel length. We here assume the extent of the interface region (δ) is small compared to the length of the channel (L), $\delta << L$. This implies that significant transverse velocities are confined to a region close to the interface, away from which streamlines are axial. The pressure-driven velocity component, U_p, supports electroosmotic flow in the higher conductivity region (Region 2) and opposes electroosmotic flow in the lower conductivity segment (Region 1). A conservation of mass gives

$$\begin{aligned}\oint_{A_o} \left(U_{p,1}\right)\mathrm{d}A + U_{\text{eof},1}A_0 &= \oint_{A_o} \left(U_{p,2}\right)\mathrm{d}A + U_{\text{eof},2}A_0 \\ &= \langle vE \rangle = V_{\text{bulk}}\end{aligned} \tag{7}$$

where the integral is over the cross-section of the channel and the < > operator indicates an axial-length-averaged quantity as in $\langle vE \rangle = \frac{1}{L}\int_0^L vE\mathrm{d}x$. This expression for bulk fluid EOF subject to non-uniform electroosmotic mobility in terms of a length-averaged liquid velocity is derived in detail by Anderson and Idol (1985). Substituting from Eq. 2 in Eq. 7, and combining with Eq. 5,

$$\oint_{A_o} \left(U_{p,2} - U_{p,1}\right)\mathrm{d}A = (\gamma v_1 - v_2)A_0E_0\frac{x_D}{(\gamma(L-x_D)+x_D)} \tag{8}$$

where, v_1 and v_2 are the electroosmotic mobility in the low and high conductivity regions respectively. Equation 8 is similar to that developed by Burgi and Chien (1991) for a finite, low-conductivity sample plug and in an otherwise uniform background electrolyte. Assuming quasi-steady flow, the average pressure-driven velocity in the low conductivity region is:

$$\bar{U}_{P1} = \frac{(\gamma v_1 - v_2)E_o x_D}{(\gamma(L-x_D)+x_D)}. \tag{9}$$

Using the above expression we can relate the local value of pressure gradient to the average velocity for various geometries. For example, for a rectangular channel with width $2a$ and depth $2b$

$$-\frac{\mathrm{d}P}{\mathrm{d}x} = \frac{3\mu\bar{U}_{P1}}{a^2\left[1 - \frac{192a}{b\pi^5}\sum_{i=1,3,5}^{\infty}\frac{\tanh(i\pi b/2a)}{i^5}\right]}. \tag{10}$$

Also, the centerline pressure-driven velocity can be related to the average velocity for a rectangular channel as:

$$U_C = \frac{48}{\pi^3}\left(\frac{\sum_{i=1,3,5}^{\infty}\frac{(-1)^{(i-1)/2}}{i^3}\left[1 - \frac{1}{\cosh(i\pi b/2a)}\right]}{\left[1 - \frac{192a}{b\pi^5}\sum_{i=1,3,5}^{\infty}\frac{\tanh(i\pi b/2a)}{i^5}\right]}\right)\bar{U}_{P1} \tag{11}$$

Lastly, we can obtain a relation between x_D versus time. The interface between conductivity segments sweeps the channel at the velocity given by Eq. 7 so that $\mathrm{d}x_D/\mathrm{d}t = V_{\text{bulk}}$.Since the electric field is assumed uniform within a segment but changing with time as the interface sweeps the microchannel, we write

$$\begin{aligned}\frac{\mathrm{d}x_D}{\mathrm{d}t} &= \frac{1}{L}\left[\int_0^{x_D} v_2E_2\mathrm{d}x + \int_{x_D}^{L} v_1E_1\mathrm{d}x\right] \\ &= \frac{1}{L}\left[v_2E_2x_D + v_1E_1(L-x_D)\right]\end{aligned} \tag{12}$$

Substituting from Eq. 5,

$$\frac{\mathrm{d}x_D}{\mathrm{d}t} = \frac{E_0}{(x_D + \gamma(L-x_D))}\left[v_2x_D + \gamma v_1(L-x_D)\right]. \tag{13}$$

Equation 13 is integrated to yield a relation for the time for the front to sweep the channel length:

$$t = \frac{1}{E_0}\left[\frac{(\gamma-1)}{(\gamma v_1 - v_2)}x_D + \frac{\gamma L(v_2 - v_1)}{(\gamma v_1 - v_2)^2}\ln\left\{1 + \frac{(v_2 - \gamma v_1)}{\gamma L v_1}x_D\right\}\right] \tag{14}$$

The variables in Eq. 14 are the electroosmotic mobilities, v_1 and v_2; the ratio of conductivities, γ; the length of the high conductivity segment, x_D; and the undisturbed/characteristic electric field, E_0. γ, E_0 and the length of the channel, L are prescribed by the experimental conditions. Note that dependence on the channel cross-

sectional area has dropped out and the result is valid for any long thin tube of arbitrary cross-sectional area shape and purely axial conductivity gradients. Equation 14 is non-dimensionalized with $L/(v_1 E_0)$, L, and v_1 for t, x_D, and v_2, respectively, to yield

$$t^* = \left[\frac{(\gamma-1)}{(\gamma-v^*)}\alpha + \frac{\gamma(v^*-1)}{(\gamma-v^*)^2}\ln\left\{1+\frac{(v^*-\gamma)}{\gamma}\alpha\right\}\right]. \quad (15)$$

α may then be substituted in Eq. 9 to obtain the development of internally generated pressure-driven flow velocity components with time. This pressure-driven flow component can be obtained directly from μPIV measurements as it affects only the curvature (not the absolute off-set value) of velocity profiles. Below we present a quantification of these pressure-driven flow components and we present comparisons with the simple 1D model.

4 Experiments

Experiments were conducted in a 40 mm long glass capillary with a 100 × 100 μm square internal cross-section (Wilmad Industries). A schematic of the experimental setup is shown in Fig. 2. The capillary was imaged using an upright epifluorescent microscope with a plan apochromat (Nikon) 60× objective lens with a numerical aperture of 1.4. The field of view was centered on the axial center of the channel ($x = 0.5L$), with the object plane 50 μm from the bottom of the 100 μm deep microchannel. Illumination was provided by a dual head Nd:YAG laser (New Wave, Minilase System). The 532 nm laser beam was directed into a custom filter assembly. The microscope filter cube consisted of a 532 nm exciter filter, a dichroic beam splitter with a cut-on wavelength of 545 nm, and a 555 nm long-pass barrier emission filter. The images were recorded onto a cooled interline CCD camera (Roper Scientific Micromax). The camera had a 1,300 × 1,040 pixel array with square pixels 6.7 μm on a side. We used two by two on-chip pixel binning during image acquisition. The time between images for velocity correlations ranged from 5 to 20 ms; and the time period between success image pairs was 1.0 s. Working fluids were seeded with carboxylate-modified 1 μm fluorescent polystyrene particles (Molecular Probes) to an initial volume density of 0.05%. The particles had a peak excitation wavelength of 540 nm and a peak emission wavelength of 560 nm.

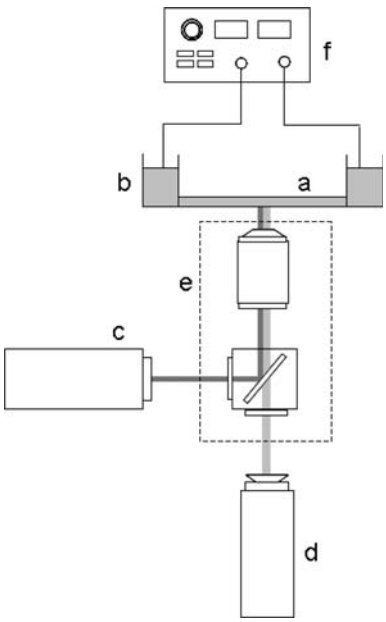

Fig. 2 Experimental setup for FASS experiments. A borosilicate capillary (**a**) with a square cross-section (100 μm × 100 μm ID) and a length of 40 mm is coupled to 500 μl reservoirs (**b**) on either end. Illumination is provided by a dual-pulse Nd:YAG laser (**c**) with a nominal energy per pulse of 1 mJ. Particle images are recorded onto a high-resolution interline transfer CCD camera (**d**) using an epifluorescence microscope (**e**). A high voltage power supply (**f**) provides a static potential to one electrode and the other electrode is grounded

The low conductivity electrolyte was 10 mM HEPES buffer (pH = 7.2, σ = 0.2 mS/cm). For the higher conductivity electrolyte, we added KCl to the 10 mM HEPES solution; the pH of the two electrolyte segments were the same. Both buffers were filtered with a 0.2 μm filter prior to loading the spheres.

The electrokinetic flow was driven by a high voltage power supply (Hewlett-Packard) using platinum electrodes inserted into end-channel wells (i.e., reservoirs) about 500 μl in volume. The channel and both the reservoirs were initially filled with the low conductivity buffer. The interface was created by removing the contents of one well with a syringe and then pipetting in the second buffer of higher conductivity.

5 Results and discussion

The flow field is monitored at an imaging location fixed in space which observes first the flow in the low conductivity electrolyte and then, after the conductivity interface sweeps by, the flow in the high conductivity electrolyte. In all of our plots, the interface sweeps in from left to right. Particle displacement fields are obtained near the center of the capillary before, during and after the interface sweeps through the imaging region. Particle velocities reflect the sum of local liquid velocity (electroosmotic, U_{eof} and pressure driven, U_p, components) and local particle electrophoretic velocity U_{eph}) (Devasenathipathy et al. 2002) $U_{\text{particle}} = U_{\text{eof}} + U_{\text{eph}} + U_p$.

The electroosmotic and electrophoretic components of the total velocity field are a uniform (DC-type) offset to the

total velocity profile and do not contribute to the curvature of the profile (at least in the regions away from the interface). Within the elongated/dispersed interface, the measured flow fields exhibit a two-dimensional transition region as the pressure gradient changes direction. The electric field away from the interface can be assumed uniform across the height of the channel and the electroosmotic and electrophoretic velocity components are assumed to have no gradients perpendicular to the flow. In these regions, the curvature in the flow field is due to the generated, internal pressure gradient $(\partial U_{\text{particle}}/\partial y = \partial U_p/\partial y \neq 0)$. Away from the interface, the curvature of the velocity profile contains only pressure-driven flow information.

Particle velocity fields obtained in a single experiment using μPIV are shown in Fig. 3. Figure 3a shows the velocity field in the leading low conductivity region where an adverse pressure gradient drives a flow opposing electroosmosis. Figure 3b shows the favorable pressure gradient assisting electroosmotic flow in the trailing high conductivity zone. Each measurement is for one image pair. We used interrogation regions 128 pixels in the horizontal direction and 32 pixels in the vertical direction with 50% overlap in both directions. Figure 4a clearly shows the adverse and the subsequent favorable (Fig. 4b) pressure gradients of the FASS flow field. The adverse pressure gradient increases in magnitude as the interface moves along the channel and the fraction of the channel length occupied by the higher conductivity electrolyte increases.

The temporal evolution of the dimensional centerline velocity versus time for a fixed γ of 20 and three different electric fields (E = 50, 100 and 150 V/cm) is plotted in Fig. 4a. One hundred image pairs were interrogated to yield each data set. The pressure-driven centerline velocity at $x_D = 0.5L$ are 450, 1,080 and 1,550 μm/s for electric field strengths of 50, 100 and 150 V/cm, respectively. The measurements follow the expected trend of a growing

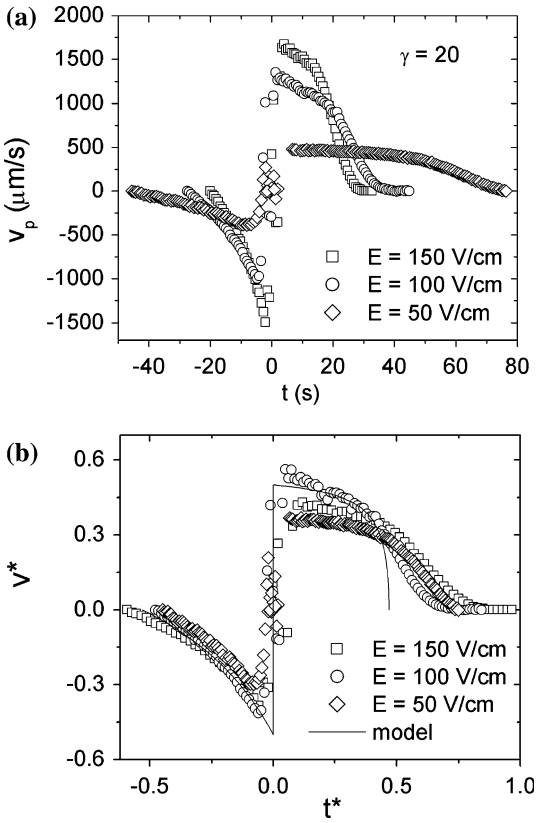

Fig. 4 Centerline pressure driven velocity in microchannel for **a** γ = 20 for electric field strengths of 50, 100, and 150 V/cm and **b** model predictions plotted shown together with experimental data for non-dimensionalized centerline velocity and non-dimensionalized time. The abscissa for the model and the non-dimensionalized data has been centered at zero when the interface sweeps past the field of view. The velocity on the ordinate is non-dimensionalized by the magnitude of the velocity discontinuity as predicted by the one-dimensional model and the time on the abscissa is non-dimensionalized by the time that the model predicts for the interface to sweep the channel length

adverse pressure gradient in the low conductivity zone and changing to a favorable pressure gradient as the interface moves past the field of view. For fixed γ, the velocity scales

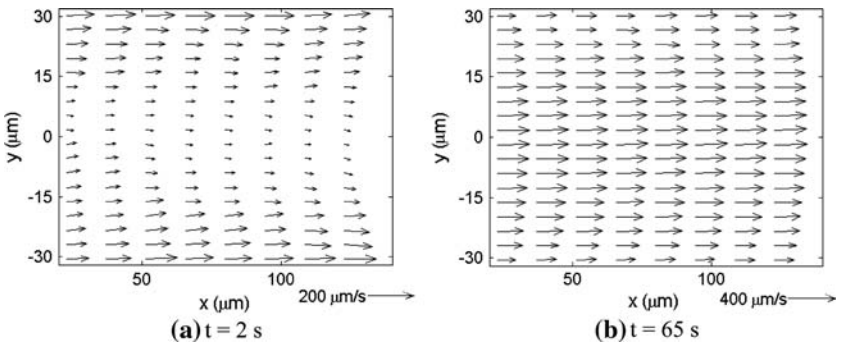

Fig. 3 Representative velocity field measurements for FASS for a stacking ratio of γ = 20 and an applied nominal field of E = 50 V/cm (applied from left to right). Vector fields at two time instances are shown. **a** The adverse pressure gradient drives a flow opposed to electroosmosis; **b** a favorable pressure-driven flow adds to electroosmosis in the trailing, higher conductivity zone (after the conductivity interface has swept past)

with the electric field. The dimensional centerline velocity versus time for a fixed electric field and three different γ is plotted in Fig. 5a. The uncertainty associated with the velocity measurements in the unstacked region (away from the interface) is approximately 10%. This error was estimated via a propagation of error analysis (Coleman and Steele 1989), and includes errors due to Brownian motion, errors in displacement measurement via cross-correlation, particle-to-particle differences in electrophoretic mobility, and possible velocity gradient error associated with the $\pm\delta z_m/2$ measurement depth (Meinhart et al. 2000; Olsen and Adrian 2000).

We extract the pressure driven velocity component (and associated estimate of local pressure gradient) from the measured velocity fields (e.g. Fig. 3a, b) by fitting an analytical function for the expected velocity vector field at each time. This approach assumes that the pressure gradient is quasi-steady over the observation time as well as uniform across the field of view. During the time interval of 10 ms between the image pair for the velocity correlations, the conductivity interface travels less than 0.5% of the total channel length. This causes negligible change in pressure gradients over the observation time. Also, the field of view is 150 μm, while the interface between low and high conductivity is $\sim$2 mm long, so the pressure gradient can be assumed to be spatially uniform over the field of view. We approximate the centerline velocity distribution (axial velocity, u, vs. y) as a parabola. (This approximate parabolic profile for the midplane, $x = 0$, velocity distribution is approximately 2% different than the fully-developed, pressure-driven flow profile for this square cross section channel geometry White (1991)). The regression coefficient for our fits ranged from 0.82 (in the low velocity regions) to 0.97 (in the high velocity regions), with a typical value of 0.9. The pressure gradients from each velocity field are arithmetically averaged to obtain an area-averaged pressure gradient estimate. We estimate that the uncertainty in the mean of this distribution is approximately 6 and 2% based on the Student's t-distribution, for the velocity profiles shown in Fig. 3a, b.

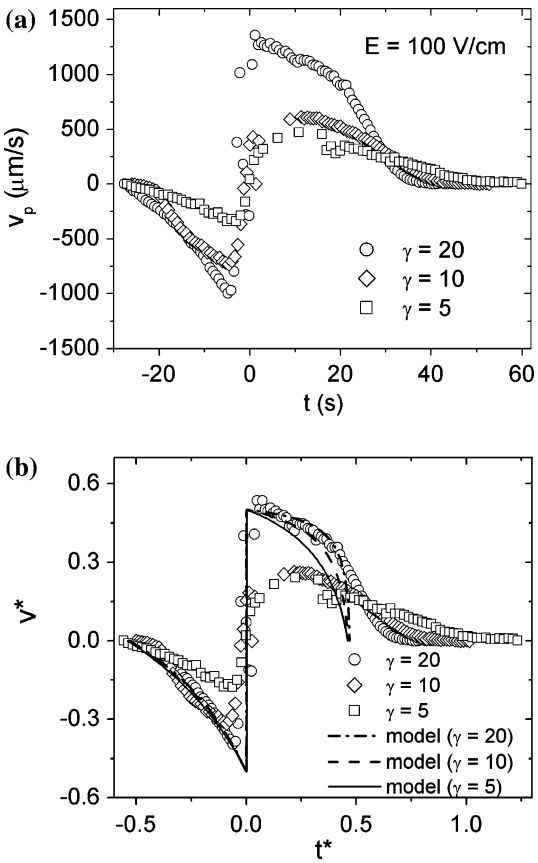

Fig. 5 Centerline pressure driven velocity in microchannel for **a** electric field strengths of 100 V/cm and conductivity ratios, γ of 5, 10 and 20. **b** Model predictions (together with experimental data) plotted with non-dimensionalized centerline velocity and non-dimensionalized time. The abscissa for the model and the non-dimensionalized data has been centered at zero when the interface sweeps past the field of view

Figures 4b and 5b show the 1-D model predictions compared with the non-dimensionalized data from Figures 4a and 5a. The two quantities of interest which are used to non-dimensionalize the centerline pressure driven velocity component, v_p and time are Δv, the centerline velocity jump as the interface sweeps past the field of view and Δt, the time taken by the front to traverse the length of the channel, respectively. These two quantities are functions of four parameters: γ, α, v_1, and v_2/v_1. The value of γ is obtained from an apriori measurement of the conductivity of the sample buffers used in the experiment (conductivity meter, Jenco). α is the distance that the interface has traversed and is obtained as a function of time from Eq. 15. The velocity difference/jump (defined as maximum minus the minimum centerline velocity) can be estimated from Eq. 11. The value of v_1 is the electroosmotic mobility for borosilicate capillaries. The ratio, v_2/v_1 was taken from Bharadwaj and Santiago (2005) As such, the scaling presented here is performed with no fitting parameters and is predicted solely from the model and independent measurements of the relevant parameters. The model captures the major trends of the dynamics and, to some degree, the dependence on field and conductivity ratio.

The 1-D model does not, of course, predict the finite extent of the interface. Also not captured by the model is the tailing off of the pressure driven velocity component as the interface exits the channel. The exit of the (finite width) interface from the long thin channel into the large volume of the downstream reservoir is described by a more complex three-dimensional flow field.

There are several other subtleties not captured by our simple model, and they are worth pointing out here as they can potentially impact practical considerations of microfluidic electrokinetic systems with heterogenous electrolytes. First, we neglect the two- and three-dimensional velocity field within the conductivity interface. This results in some discrepancy between model and data for data within the interface, as shown in Figs. 4 and 5. Second, we did not address the finite temporal response of EOF mobility to abrupt changes in local ion density. Electroosmotic mobility transients of a channel subject to abrupt changes in concentration are known to have both short and long time scales (e.g., minutes to days) (Hunter 1981; Raviv et al. 2002). One insight offered by our data is that at least some component of the change in mobility for changes in concentration acts very quickly, within a few seconds. Presumably, this is due at least to the adjustment of the diffuse ion portions of the double layer to local ion density. Third, consider that the particle density field is originally homogeneous but quickly becomes heterogenous. This is due to the fact that the charged particles are themselves stacked in the flow field.[1]

The particles near the interface (especially immediately to the left of the interface) therefore experience unsteady local ion concentrations, and so transients in particle mobilities may become important. Lastly, consider that there is some uncertainty in the initial condition of the interface as it was created by removing the low conductivity buffer from the upstream reservoir and manually injecting the high conductivity buffer. This manual buffer exchange is expected to result in a somewhat distorted initial interface between the buffers.

In summary, the data demonstrates that the flow has strong transients in the local velocity field and is strongly affected by unsteady, non-uniform velocity fields created by gradients in the electroosmotic slip velocity. These gradients in slip velocity are attributable to (and the data is consistent with) the effect of local ion density on electroosmotic mobility. Further, the simple 1D model presented here is useful in predicting the general properties of the flow including its time and velocity scales and the trends across conductivity ratio and electric field magnitude. More general treatment of the problem would probably require solutions to two- or three-dimensional transport equations, and may require further study of the transient response of wall and particle electrokinetic mobilities.

[1] An ideal flow tracer would have zero electrophoretic mobility, but stability of the seed particle colloidal dispersion depends largely on surface charge. Aqueous solutions of uncharged particles, if realizable, are expected to suffer from particle flocculation, adsorption to the walls, and perhaps precipitation.

6 Conclusions

This paper presents the first experimental investigation of the FASS velocity flow field. We used charged polystyrene spheres and μPIV measurements to quantify velocity fields. Experiments were conducted in a straight microcapillary geometry with a square cross-section 100 μm on a side. μPIV measurements yield particle velocity fields in these heterogeneous, unsteady electrokinetic flows. The temporal development of the velocity field was captured as the single electrolyte–electrolyte interface sweeps across the length of the channel. A simple 1D model was proposed that captures the trends of the temporal evolution of the internal pressure gradient generation. The model results are compared with experiments for several conductivity ratios ($\gamma = 5$, 10, 20 and 50) and across several electric fields (E = 50, 100 and 150 V/cm). The model well captures the qualitative features of the observed dynamics as well as quantitative experimental quantities such as the magnitude of generated internal pressures (order 1 mm/s pressure component velocities are generated), the velocity of the electrolyte interface, and the shape of the short-time and transition period during which the interfaces occupies the center regions of the channel. The model shows only fair agreement with the dynamics of the longer-term decay of the pressure gradient as the conductivity interface approaches the channel exit. This discrepancy may be due to the fact to the effects of the three-dimensional flow field which describes the exit of the (finite, increased width) interface region into the downstream reservoir. Also important may be the finite temporal response of EOF mobility to abrupt changes in local ion density—an effect which merits further study.

The velocity profiles obtained with μPIV complement theoretical efforts that aim to develop a fundamental understanding of sample dispersion due to axial gradients in electrolyte conductivity. These particle-based imaging measurements provide temporally and spatially resolved measurements of particle velocities in a complex heterogenous flow field. Velocity field measurements can therefore potentially provide valuable data and insight that complement scalar dye-based imaging techniques. The results also provide benchmark data for efforts to model heterogenous, unsteady electrokinetic flows.

References

Anderson JL, Idol WK (1985) Electroosmosis through pores with nonuniformly charged walls. Chem Eng Commun 38:93–106

Bharadwaj R, Santiago JG (2005) Dynamics of field-amplified sample stacking. J Fluid Mech 543:57–92

Burgi DS, Chien RL (1991) Optimization in sample stacking for high-performance capillary electrophoresis. Anal Chem 63(18):2042–2047

Chen CH et al (2005) Convective and absolute electrokinetic instability with conductivity gradients. J Fluid Mech 524:263–303

Chien RL, Burgi DS (1991) Field amplified sample injection in high-performance capillary electrophoresis. J Chromatogr 559(1–2):141–152

Chien R, Burgi D (1992) Sample stacking of an extremely large injection volume in high-performance capillary electrophoresis. Anal Chem 64(9):1046–1050

Coleman HW, Steele GW (1989) Experimentation and uncertainty analysis for engineers, 1st edn. Wiley, New York

Devasenathipathy S, Santiago J, Takehara K (2002) Particle tracking techniques for electrokinetic microchannel flows. Anal Chem 74(15):3704–3713

Huang XH, Gordon MJ, Zare RN (1988) Current-monitoring method for measuring the electroosmotic flow-rate in capillary zone electrophoresis. Anal Chem 60(17):1837–1838

Hunter RJ (1981) Zeta potential in colloid science. Academic, London

Jacobson SC, Ramsey JM (1995) Microchip electrophoresis with sample stacking. Electrophoresis 16(4):481–486

Jacobson SC, Hergenroder R, Koutny LB, Ramsey JM (1994) High-speed separations on a microchip. Anal Chem 66(7): 1114–1118

Kasicka V et al (1997) Capillary zone electrophoresis with external radial electric field control of electroosmotic flow and its application to the separation of synthetic oligopeptides. J Chromatogr A 772(1–2):221–230

Kim MJ, Beskok A, Kihm KD (2002) Electro-osmosis-driven microchannel flows: a comparative study of microscopic particle image velocimetry measurements and numerical simulations. Exp Fluids 33(1):170–180

Lin H et al (2004) Instability of electrokinetic microchannel flows with conductivity gradients. Phys Fluids 16(6):1922–1935

Manz A, Harrison DJ, Verpoorte EMJ, Fettinger JC, Paulus A, Ludi H, Widmer HM (1992) Planar chips technology for minituarization and integration of separation techniques into monitoring systems: capillary electrophoresis on a chip. J Chromatogr 593:253–258

Meinhart CD, Wereley ST, Gray MHB (2000) Volume illumination for two-dimensional particle image velocimetry. Measure Sci Technol 11(6):809–814

Olsen MG, Adrian RJ (2000) Out-of-focus effects on particle image visibility and correlation in microscopic particle image velocimetry. Exp Fluids 29:S166–S174

Quirino J, Terabe S (1999) Sample stacking of fast-moving anions in capillary zone electrophoresis with pH-suppressed electroosmotic flow. J Chromatogr A 850(1–2):339–344

Raviv U, Laurat P, Klein J (2002) Time dependence of forces between mica surfaces in water and its relation to the release of surface ions. J Chem Phys 116(12):5167–5172

Ren CL, Li DQ (2006) Electrokinetic sample transport in a microchannel with spatial electrical conductivity gradients. J Colloid Interface Sci 294(2):482–491

Ross D, Gaitan M, Locascio LE (2001) Temperature measurement in microfluidic systems using a temperature-dependent fluorescent dye. Anal Chem 73(17):4117–4123

Sadr R et al (2004) An experimental study of electro-osmotic flow in rectangular microchannels. J Fluid Mech 506:357–367

Santiago JG (2001) Electroosmotic flows in microchannels with finite inertial and pressure forces. Anal Chem 73(10):2353–2365

Szymczyk A et al (1999) An application of the space charge model to the electrolyte conductivity inside a charged microporous membrane. J Memb Sci 161(1–2):275–285

Thormann W et al (1998) Modeling of the impact of ionic strength on the electroosmotic flow in capillary electrophoresis with uniform and discontinuous buffer systems. Anal Chem 70(3):549–562

Wainright A et al (2002) Sample pre-concentration by isotachophoresis in microfluidic devices. J Chromatogr A 979(1–2):69–80

White FM (1991) Viscous fluid flow, 2nd ed. McGraw-Hill Series. In: Holman JP, Lloyd JR (eds) Mechanical engineering. McGraw-Hill, New York, pp 614

Yang H, Chien RL (2001) Sample stacking in laboratory-on-a-chip devices. J Chromatogr A 924(1–2):155–163